Revision 1

Word Count: 9732

The effect of elemental diffusion on the application of olivine-composition-based magmatic thermometry, oxybarometry, and hygrometry: A case study of olivine phenocrysts from the Jiagedaqi basalts, northeast China

Le Zhang[1]*, Lu-Bing Hong[2], Sheng-Ping Qian[3], Peng-Li He[1], Miao-Hong He[1], Ya-Nan Yang[1], Jin-Tuan Wang[1], Yan-Qiang Zhang[1], Zhong-Yuan Ren[1]*

[1] State Key Laboratory of Isotope Geochemistry and CAS Center for Excellence in Deep Earth Science, Guangzhou Institute of Geochemistry, Chinese Academy of Sciences, Guangzhou 510640, China

[2] College of Earth Science, Guilin University of Technology, Guilin 541004, China

[3] State Key Laboratory of Marine Geology, Tongji University, Shanghai, 200092, China

*Corresponding author：

zhangle@gig.ac.cn

zyren@gig.ac.cn

This is the peer-reviewed, final accepted version for American Mineralogist, published by the Mineralogical Society of America.
The published version is subject to change. Cite as Authors (Year) Title. American Mineralogist, in press.
DOI: https://doi.org/10.2138/am-2022-8567. http://www.minsocam.org/

Abstract

Olivine compositions are widely used to constrain magmatic thermodynamic conditions such as magmatic temperature, oxygen fugacity, and H_2O content. However, elemental diffusion may change the initial compositions and lead to large uncertainty on the estimation of these thermodynamic conditions. In this study, we conducted LA–ICP–MS elemental mapping and EPMA analysis of olivine phenocrysts and olivine-hosted spinel from the Jiagedaqi (JGD) alkaline basalts in northeast China to evaluate the influence of elemental diffusion on olivine-composition-based geothermometry, oxybarometry, and hygrometry. The JGD olivines show normal Fo (Mg/(Mg + Fe) × 100 in mole) zoning, with cores having Fo of 77–87 and rims having Fo of 67–73. The constant P contents from core to rim indicate that these compositional zonings were caused mainly by diffusion. Because Al is a slow-diffusing element and its content is relatively constant from core to rim, the temperature calculated by the Al-in-olivine thermometer is not influenced by elemental diffusion and preserves the JGD olivine crystallization temperature up to 1150 °C. The temperatures calculated using the Sc/Y-in-olivine thermometer, the oxygen fugacity calculated using the olivine–spinel oxybarometer, and the H_2O content calculated on the basis of Ca partitioning between olivine and melt are strongly influenced by the diffusion of Fo, Sc/Y, and Ca. However, the compositional plateaus in olivine cores, which were not influenced by elemental diffusion, preserve the magmatic temperature (1150 °C), oxygen fugacity (QFM + 1.4), and H_2O content (4 wt.%) that applied during the formation of the JGD olivines. Together, these

findings suggest that the mantle source of the JGD basalts was metasomatized by fluids released from the subducted slab. This study highlights that elemental diffusion in olivine phenocrysts can strongly affect the application of olivine-composition-based geothermometers, oxybarometers, and hygrometers. However, primitive olivine cores that have not been influenced by diffusion preserve the initial magmatic thermodynamic conditions.

Keywords: Olivine, diffusion, magma storage, compositional zoning, NE China, Jiagedaqi basalts

Introduction

Basalt, originating from the Earth mantle, is considered as a probe to detect the composition of the deep Earth and the material recycling between Earth surface and deep spheres (Abraham et al., 2001; Fisk and Kelley, 2002; Herd, 2008; Herzberg, 2011a; Hofmann, 2003). The formation and evolution of basaltic magmas depends on various factors, such as source lithology, water content, temperature, and redox state. As olivine is an early crystallized silicate mineral from primitive basaltic magma, several recent studies have suggested that olivine chemistry may be used to evaluate these factors. For example, Ni and Mn contents and Mn/Zn ratios of primitive olivine are suggested to be controlled by source lithology and can thus be used as discriminators between pyroxenite and peridotite sources (Herzberg, 2011b; Howarth and Harris, 2017; Liu et al., 2021; Sobolev et al., 2005). The partitioning of Ca between olivines and their host magmas is affected by magmatic H_2O and can thus act as a proxy for magma H_2O content (Gavrilenko et al., 2016; Hong et al., 2017). As the partitioning of V, a multivalent element, is sensitive to oxygen fugacity (Canil, 1997; Mallmann and O'Neill, 2009; Shearer et al., 2006; Shishkina et al., 2018; Wang et al., 2019), it has been suggested that the partitioning of a ratio of V to a homovalent element (e.g., V/Sc) between olivine and silicate melt is a proxy for oxygen fugacity (Mallmann and O'Neill, 2013; Wang et al., 2019). Mallmann and O'Neill (2013) proposed an empirical thermometer based on the partitioning of Sc/Y between olivine and silicate melt. The partitioning behavior of Al between co-existing olivine and spinel can be used to reconstruct magmatic temperature (Coogan et al., 2014; Wan et

al., 2008).

To use olivine compositions as thermodynamic proxies, an assumption is that these element contents or ratios remain unchanged after the formation of olivine. However, chemical zoning in olivine is a common phenomenon, and the presence of this chemical zoning means that elemental diffusion is certain to have occurred (Albert et al., 2019; Howarth and Gross, 2019; Kahl et al., 2011; Longpré et al., 2014; Mutch et al., 2019; Ruprecht and Plank, 2013; Shea, et al., 2015a, 2015b; Thomson and Maclennan, 2013). For example, olivine crystals in the lava of the April 2007 caldera-forming eruption of Piton de la Fournaise volcano have relatively constant values of Fo of 85, Ni of 2170 ppm, and Ca of 1930 ppm in their cores, but show normal zoning in the outermost (100 μm thick) rims, in which Fo and Ni decrease to about 82 and 1650 ppm, respectively, and Ca increases to 2140 ppm (Albert et al., 2019). The diffusion profiles depend on the initial element contents, diffusion coefficients, and elapsed time. Therefore, element contents and ratios may change owing to diffusion.

The Early Cretaceous basalts from the Jiagedaqi (JGD) area, northeast (NE) China, are porphyritic and contain abundant subhedral to euhedral mm-sized olivine crystals with compositional zonation. Thus, the JGD olivine phenocrysts are great candidates to investigate the effect of elemental diffusion on the application of olivine-composition-based magmatic thermometry, oxybarometry, and hygrometry. In this study, major- and trace-elemental zoning in JGD olivine phenocrysts was investigated by laser-ablation–inductively coupled plasma–mass spectrometry (LA–

ICP–MS) and electron microprobe element mapping techniques. In this paper, we show that the elemental zoning was caused mainly by elemental diffusion and discuss the influence of this compositional zoning on element- or element-ratio-based thermometry, oxybarometry, and hygrometry.

Geological background and rock characteristics

Northeast China is located in the eastern Central Asian Orogenic Belt (CAOB), with the Siberian Craton to the north and the North China Craton (NCC) to the south (**Fig. 1a**). Northeast China consists of several Paleozoic micro-continental blocks including, from northwest to southeast, the Erguna, Xing'an, Songnen–Zhangguangcai Range, Jiamusi, and Khanka massifs, which collided and amalgamated with each other during the Paleozoic (Wilde, 2015; Wilde and Zhou, 2015; Wu et al., 2011; Xu et al., 2013). From the Paleozoic to Mesozoic, NE China was affected by the closures of the Paleo-Asian Ocean to its south and the Mongol–Okhotsk to its north (Xiao et al., 2009; Xiao et al., 2003). From the Jurassic, subduction of the Paleo-Pacific Plate beneath NE China played an important role in the geological evolution of this area (Tang et al., 2018; Xu et al., 2013).

The Jiagedaqi (JGD) area is located in the central Great Xing'an Range, in which abundant Early Cretaceous volcanic rocks are widely distributed (**Fig. 1b**). The studied JGD volcanic rocks are exposed ~65 km to the south of Jiagedaqi county and consist mainly of olivine-bearing basalts. Zircon U–Pb and Ar–Ar geochronology have shown that the volcanic rocks in the study area are of Early Cretaceous age

(Wang et al., 2006; Zhang et al., 2008a). Enrichment in light rare earth elements (LREEs) and large ion lithospheric elements (LILEs), depletion in heavy rare earth elements (HREEs) and high field strength elements (HFSEs), and the enriched Sr–Nd–Pb isotopes of the JGD basalts indicate that the mantle source of the JGD basalts was metasomatized by fluids released from a subducted slab (Fan et al., 2003; Luo et al., 2020; Zhang et al., 2008b).

The JGD basalts have a porphyritic texture, with 20–30 vol.% phenocrysts (**Fig. 2a and b**). Olivines are one of the main phenocryst phases, with grains having subhedral to euhedral shapes and measuring 0.5–2.5 mm in length. Most olivine crystals have cracks, and parts of them show weak serpentinization along rims and cracks. Euhedral spinel and primary melt inclusions occur in many olivines. Clinopyroxenes constitute the other main phenocryst phase and have short-columnar shapes and measure 0.5–2.0 mm in length. The matrix of the JGD basalts comprises small clinopyroxenes and plagioclases, with a few opaque minerals. A more detailed petrographic description and geochemical characteristics (major and trace elements and Sr–Nd–Pb isotopes) of the JGD basalts have been reported by Luo et al. (2020). The olivine selection guidelines proposed by Shea et al. (2015a), avoiding small grains, away from crystal corners, with clear concentration plateau, were followed to select olivine crystals for elemental profile analyses.

Analytical methods

Major- and trace-element mapping of olivine by LA–ICP–MS

Major- and trace-element mapping of olivine was conducted using a 193 nm ArF excimer LA system (RESOlution M50, Resonetics, USA) coupled to a sector-field ICP–MS instrument (ELEMENT XR, Thermo Fisher, USA) housed at the State Key Laboratory of Isotope Geochemistry, Guangzhou Institute of Geochemistry, Chinese Academy of Sciences (SKLIG–GIG–CAS), Guangzhou, China. Detailed descriptions of the two instruments have been reported in previous studies (Zhang et al., 2021; Zhang et al., 2019). The RESOlution M50 LA system has a two-volume LA cell (Laurin Technic), which enables the system to wash out 99% of the signal in less than 1.5 s (Müller et al., 2009). Element mapping was conducted on standard 30-μm-thick polished rock thin-sections, mounted in an in-house rotatable holder. By adjusting the longitudinal direction of the measured olivine crystal parallel to the X or Y axis, this rotatable holder ensures that a minimum rectangle measurement area envelops the whole crystal and thus improves the measurement efficiency. Before analysis, the surfaces of thin sections were cleaned with ethanol and deionized water and then dried with a nitrogen gun. A series of parallel rasters across the olivine crystal surface were ablated to form a rectangular grid (**Fig. 2c and d**). The measured raster lines were arranged in successive order, with no gaps or overlaps between each other. The laser was operated with a 45 μm beam size, 15 Hz repetition rate, 8 J cm^{-2} energy density, and 10 μm s^{-1} moving speed for edge-to-edge sampling. Pre-ablation of each raster was used to remove any contamination on sample surfaces, and each raster started with 20 s gas blank measurement with the laser off.

The ELEMENT XR sector-field ICP–MS was set to low mass resolution mode.

Signals of the following masses were detected in olivine: ^{7}Li, ^{23}Na, ^{27}Al, ^{25}Mg, ^{29}Si, ^{31}P, ^{43}Ca, ^{45}Sc, ^{47}Ti, ^{51}V, ^{53}Cr, ^{55}Mn, ^{57}Fe, ^{59}Co, ^{60}Ni, ^{63}Cu, ^{66}Zn, ^{71}Ga, ^{89}Y, and ^{90}Zr. Dwell time and settling time for each mass and other instrumental parameters are given in **Table S1**. The total sweep time from ^{7}Li to ^{90}Zr was 0.55 s. Under these instrumental settings, the total analysis time was approximately 2 h for an area of 1.5 mm × 1.5 mm on the sample surface. The oxide molecular yield (^{232}Th^{16}O/^{232}Th) was less than 0.3%. United States Geological Survey (USGS) reference glass GSD-1G was used as the external calibration material, and BHVO-2G and an in-house olivine standard (JHOL) were measured as unknown samples to evaluate the analytical precision and accuracy. Element mapping of every five unknown samples was preceded and followed by one analysis of GSD-1G. For olivine crystals, the sum of all measured metal oxides was normalized to 100% to calculate the content of each element (Liu et al., 2008; Wu et al., 2020). The limits of detection (LODs) for all measured elements were estimated from the counting statistics of the gas blank intensities and are listed in **Table S2**. An in-house written Python 3 software program, *Fastline*, was used to process element content calibration and create elemental pseudo color plots.

Olivine and spinel composition analyses using an electron microprobe

Compared with LA–ICP–MS, electron probe microanalysis (EPMA) has a higher spatial resolution (beam size of several micrometers for EPMA vs. tens of micrometers for LA–ICP–MS) and is more accurate and precise for major elements.

Core to rim concentration profiles for the elements Si, Mg, Fe, Ni and Ca of 20 olivine crystals were measured using a Cameca SXFive FE EPMA at SKLIG–GIG–CAS. The operating conditions were 20 kV accelerating voltage, 100 nA beam current, and 1 μm beam size. The step interval between two adjacent points was about 20 μm. Si, Mg, Fe, Ni, and Ca were detected using LTAP, LTAP, LIF, LLIF, and LPET crystals, respectively. Major-element compositions (Si, Mg, Al, Mn, Fe, Cr, and Ti) of spinel inclusions in olivine phenocrysts and of their olivine hosts (Si, Mg, Fe, and Al) were also measured with EPMA. All spinel grains selected for analysis are close to the cores of their olivine hosts (**Fig. S1**). The operating conditions for spinel were a beam current of 20 nA, a beam diameter of 1 μm, and an accelerating voltage of 15 kV. For olivine, the operating conditions were a beam current of 100 nA, a beam diameter of 2 μm, and an accelerating voltage of 20 kV. MongOl olivine (Batanova et al., 2019) and spinel standard BAR8601-10 (Cao et al., 2019) were used to monitor the accuracy and precision of the measurements. Repeated analyses of both standards show that the relative standard deviation (2RSD) for most elements is 0.1%–1.2%, for CaO is 5.8%, and for Al_2O_3 (in olivine) is 6.6% (Table S5).

Electron backscattered diffraction mapping

Electron backscattered diffraction (EBSD) mapping was performed to obtain the crystallographic orientation of olivine at the State Key Lab of High Performance Ceramics and Superfine Microstructure, Shanghai Institute of Ceramics, CAS, using an FEI Magellan 400 field-emission scanning electron microscope (SEM) equipped

with a Channel 5 EBSD system (Oxford Instruments) and a Nordly-S EBSD detector. Detailed analytical procedures have been reported by Wang et al. (2017). Instrumental conditions were an accelerating voltage of 15 kV, a working distance of ~5 mm, and a sample tilt of 70°.

ANALYTICAL RESULTS

Olivine compositions and zoning profiles

Twenty olivine crystals were selected for major and minor element measurements from rim to core by EPMA (**Table S3**). To better constrain the populations of the compositions of olivine cores and rims, ten more olivine crystals were measured their cores and rims (Table S4). The rim to core traverses show that many crystals are characterized by compositional plateaus in their cores (**Fig. 3**) and that the plateau range increases with increasing crystal size. The Fo content of olivine cores varies from 77 to 87, with a main population around Fo = 83.7 (**Fig. 4**). Compared with the wide variation of olivine cores, olivine rims have limited variation in Fo content (67–73, **Fig. 4**). One olivine crystal was selected for major- and trace-element mapping by LA–ICP–MS (**Fig. 2d**). **Figure 5** displays two-dimensional Fo, Li, Mn, Ni, Sc, Zn, Y, and V distributions in the selected olivine crystal, which indicate normal Fo zoning (Fo decreasing from core to rim). From core to rim, Ni (from ~710 ppm to 1350 ppm) decreases and Li (from ~2 ppm to 12 ppm), Mn (from ~730 ppm to 3350 ppm), V (~4 ppm to 15 ppm), Sc (~10 ppm to 14 ppm), Zn (~80 ppm to 190 ppm), and Y (~0.15 ppm to 0.75 ppm) increase. In contrast, Al_2O_3 (~0.03

wt%) and P_2O_5 (~0.2 wt%) are essentially uniform from core to rim, showing little zoning (**Fig. 6a** and **b**). Sc/Y is ~50 in the core and changes to ~20 in the rim (**Fig. 6b**).

Spinel compositions

A total of 52 JGD spinel inclusions hosted in olivines and their host olivines were analyzed for major elements (**Table S5**). Cr# values (Cr/[Cr + Al] × 100 in mol.%) vary from 32 to 41 and the Fo values of their host olivines vary from 75 to 87 (**Fig. 7**). TiO_2 ranges from 0.5 to 3.1 wt.% and displays little correlation with Cr#. Al_2O_3 content varies from 25 to 36 wt.%.

DISCUSSION

Genesis of the primitive olivine cores

Before using the primitive olivine cores to constrain the thermodynamic conditions (e.g., temperature and oxygen fugacity) of the JGD magma, the genesis of these olivine cores first needs to be established. Most JGD olivines have euhedral shapes, different from mantle xenocrysts, which normally have anhedral shapes (Kamenetsky et al., 2006; Hong et al., 2012). The high Ca contents (> 720 ppm, **Fig. 8a**) of the JGD olivines also indicates that they are not mantle-derived xenocrysts but crystallized from magma (e.g., Hong et al., 2013; Simkin and Smith 1970). In addition, the abundant primary melt inclusions hosted in JGD olivines support a magmatic origin of these olivines (**Fig. S2**; Schiano, 2003). The fractional crystallization trend of Cr#

in spinels vs Fo in their host olivines (**Fig. 7**) and the continuous compositional variations of all the measured primitive olivine cores (**Fig. 8**) suggest that these cores share the same trends of evolution and crystallized from the same magma system.

Origin of the olivine zoning

There are several possible types of zoning (Costa et al., 2008; Oeser et al., 2015, Shea et al., 2015b): inherited xenocryst cores overgrown by magmatic rims, crystal growth zoning and diffusion zoning. The first situation can be identified by the sharp contrast compositions between core and rim. The other two situations also have different geochemical features, as follows. First, if elemental zoning is caused by crystal growth, then both fast-diffusing and slow-diffusing elements should have corresponding zonings. In contrast, if zoning is caused by diffusion, the elements with different diffusion coefficients will have different diffusion profiles, and the slowest-diffusing trace element (e.g., P in olivine, CaAl-NaSi in plagioclase) may have no diffusion-induced chemical zoning (Costa et al., 2008; Neave et al., 2014; Yang et al., 2019). Second, diffusions for many elements are anisotropic in different crystallographic directions. If zoning is caused by diffusion, then the diffusion distances will vary according to different crystallographic direction (e.g., Qian et al., 2008). Third, if zoning is caused by diffusion, and the diffusion distance is much smaller than the crystal size, then the diffusion profile can be reproduced by the one-dimensional diffusion model for a semi-infinite medium with a source-maintained constant concentration (Cherniak and Watson, 1994). For the JGD olivine phenocrysts

measured in this study, contents of the fast-diffusing elements (e.g., Mg, Fe, Li, and Ni) show zoning (**Fig. 5**), whereas contents of the slow-diffusing elements (e.g., Al and P) show limited variations across olivine crystals (**Fig. 6, Table S3**). The limited variations of Al and P do not change continuously from core to rim like the fast-diffusing elements (e.g., Mg, Ca, Mn) and are mainly caused by cracks in olivine. The compositional profiles (Fo, Ni) of the JGD olivines are well reproduced by the one dimensional diffusion model for a semi-infinite medium (see discussion below). The above two lines of evidence indicate that elemental zonings in the JGD olivine phenocrysts were caused by diffusion.

Numerous studies have discussed the formation of chemical zoning in mineral phenocrysts (Albert et al., 2019; Boro et al., 2021; Costa et al., 2008; Costa and Dungan, 2005; Costa et al., 2020; Girona and Costa, 2013; Gordeychik et al., 2020; Kahl et al., 2011; Lynn et al., 2017, 2018; Shea et al., 2015b). The JGD olivine phenocrysts have normal Fo zoning, whereby the cores have primitive compositions (Fo = 77–87) and the rims have evolved compositions (Fo = 67–73). Two possible magmatic scenarios can explain the chemical zoning of the JGD olivine phenocrysts. Scenario 1: The JGD olivine cores record a pre-existing magma plumbing system and the large variations of their Fo represent different magma evolving stages. The early crystallizing olivine has higher Fo and the later crystallizing olivine has lower Fo. Later, another evolved magma recharges into the plumbing system and captures the pre-existing olivines crystallized at different stages. As rims with an evolved composition formed, element diffusion started in these olivine crystals. Subsequently,

the mixed magma was erupted, and the olivine crystals preserved the compositional zoning. Scenario 2: The JGD olivine cores, with higher Fo, crystallized from a deep magma, which carried the JGD primitive olivine and mixed with a shallower and evolved magma. Then the newly formed rims of the JGD olivine have lower Fo. Since no reverse-zoned olivine was observed in the JGD basalts, the evolved magma was possibly crystal free. Otherwise, some of the JGD olivines should have reverse zoning (Fo increase from core to rim).

Timescale for eruption of the Jiagedaqi magma

Element diffusion profiles are a useful tool for establishing the timescale of the evolution of magmatic systems (Brenna et al., 2018; Costa et al., 2008, 2020; Kahl et al., 2011; Lynn et al., 2017; Oeser et al., 2015; Shea et al., 2015a). Here, to evaluate the timescale, we used the one-dimensional diffusion model for a semi-infinite medium with a source-maintained constant concentration at a fixed crystal–melt boundary and a constant diffusion coefficient.

Finding the initial and boundary conditions

To conduct the modelling, initial and boundary conditions, which refer to the shape of the zoning pattern before modification by diffusion, should be identified first. The plateau compositions in cores of olivine phenocrysts show no gradient and were treated as the initial compositions. We used two ways of fixing the initial composition of the rim: 1) If plateaus existed near the rims, then the plateau compositions were

This is the peer-reviewed, final accepted version for American Mineralogist, published by the Mineralogical Society of America.
The published version is subject to change. Cite as Authors (Year) Title. American Mineralogist, in press.
DOI: https://doi.org/10.2138/am-2022-8567. http://www.minsocam.org/

treated as the initial compositions; and 2) if rims had no compositional plateaus, then we used the $erfc^{-1}\left[\frac{C_x - C_0}{C_i - C_0}\right]$ vs x plot to fit the initial compositions, where C_x is the concentration at distance x, C_0 is the initial concentration, C_i is the concentration at the interface (x = 0). The fitted line of $erfc^{-1}\left[\frac{C_x - C_0}{C_i - C_0}\right]$ vs x should cross the coordinate origin and to determine the initial composition (C_i), C_i is changed until the intercept of the fitted line is zero (Cherniak and Watson, 1994).

Diffusion coefficient

The Fe–Mg diffusion coefficient in olivine is a function of temperature, pressure, composition, crystallographic direction, and oxygen fugacity, as established from experimental measurements (Costa and Dungan, 2005; Dohmen et al., 2007; Petry et al., 2004). In this study, temperature and oxygen fugacity were determined using the Al-in-olivine thermometer (Coogan et al., 2014; Wan et al., 2008) and the olivine–spinel oxygen barometer (Ballhaus et al., 1991), respectively. We used temperature estimated from olivine rim compositions rather than that estimated from olivine core compositions. This is because although high-Fo olivine cores crystallized from high temperature, these high-Fo olivine were captured by an evolved magma, which had lower temperature. Because there is no spinel-olivine pair in the matrix of the JGD basalts for us to calculate the temperature of the evolved magma, we regressed a relationship of crystallization temperature vs Fo value of olivine based on Al-in-olivine thermometer (**Fig. S3)**. Using this relationship, the extrapolated temperature

for the averaged olivine rim composition (Fo = 69.46) is 1092 ℃, which was used in the calculation of Fe–Mg diffusion coefficient. The averaged oxygen fugacity based on the olivine–spinel oxygen barometer is QFM + 1.38 and was chosen for Fe–Mg diffusion coefficient calculation. Crystallographic directions were measured using EBSD (**Fig. S4**). Then, the diffusion coefficients were calculated with the DIPRA program (Girona and Costa, 2013), which was based on the formulas of Dohmen et al. (2007) and Dohmen and Chakraborty (2007). The DIPRA is a user-friendly program to model multi-element diffusion in olivine (Girona and Costa, 2013). To use DIPRA, the user needs to input an element concentration profile as a two-dimensional array, temperature, pressure, fugacity and crystal orientation.

Twenty traversing concentration profiles of the JGD olivine phenocrysts were measured to constrain the timescale (**Fig. 3 and 9** and **Table S3**) with the DIPRA program. The timescales calculated from Fo profiles range from 66 to 491 days (**Table S6**). The large variation of the calculated timescales may be due to some of the measured olivine sections do not cross through their crystal centers. This is because that if the section does not cross through the center of the measured crystal, the measured diffusion profile will be shorter than the actual profile, resulting in under estimation of the diffusion timescale. We also modeled the timescales by 17 NiO profiles (Figure 8, Table S3) of the same olivines used for timescale modelling by Fo profiles, which have a range from 76 to 588 days, generally larger than that modelled by Fo profiles ((**Fig. S5, Table S6**). This may be due to the mismatch between Fo and Ni diffusion coefficients under relatively low temperature and the less well

360 characterized diffusion coefficient of Ni compared to diffusion coefficient of Fo
361 (**Lynn et al., 2017**). The larger analytical error of Ni than Fe-Mg may also lead to
362 larger uncertainty of the timescales. Based on the above reasons, although the
363 modelling results by both Fo and NiO profiles are in a same order of magnitude
364 (dozens of days to less than two years), the timescales derived from Fo profiles are
365 preferred in this study.
366

367 **The effect of elemental diffusion on the application of olivine-composition-based**
368 **magmatic thermometry, oxybarometry, and hygrometry**

369 **Olivine crystallization temperature**

370 Temperature is a fundamental property of magmas and can be used to identify
371 their tectonic setting (Coogan et al., 2014; Herzberg and Asimow, 2008; Herzberg,
372 2011a; Putirka, 2005). In this study, two geological thermometers, the Al-in-olivine
373 thermometer (Coogan et al., 2014; Wan et al., 2008) and the Sc/Y partitioning
374 thermometer (Mallmann and O'Neill, 2013), were used to calculate the olivine
375 crystallization temperature and evaluate the influence of elemental diffusion on both
376 thermometers. The Al-in-olivine geothermometer (Coogan et al., 2014; Wan et al.,
377 2008), which is based on the partitioning of Al between coexisting olivine and spinel,
378 was first established with experiments conducted under reducing conditions (~QFM–
379 1.5) by Wan et al. (2008). Recently, Coogan et al. (2014) expanded this
380 geothermometer to more oxidized conditions using the following equation:

This is the peer-reviewed, final accepted version for American Mineralogist, published by the Mineralogical Society of America.
The published version is subject to change. Cite as Authors (Year) Title. American Mineralogist, in press.
DOI: https://doi.org/10.2138/am-2022-8567. http://www.minsocam.org/

$$T(K)=\frac{10000}{0.577+0.884Cr\#-0.897\ln(Kd)} \quad (1)$$

where $Kd=\frac{Al_2O_3^{olivine}}{Al_2O_3^{spinel}}$. This geothermometer is independent of the melt composition, crystallization pressure, and oxygen fugacity, and the uncertainty of the estimated temperature is <30°C (Coogan et al., 2014). Given that Al^{3+} diffuses in the olivine lattice far more slowly than Mg^{2+} and Fe^{2+} (Spandler and O'Neill, 2010), the Al content can still record the initial olivine crystallization temperature.

The Sc/Y partitioning thermometer was calabrated with a series of experiments under pressure of 1 bar to 2.0 GPa and temperature of 1200 – 1530 ^{o}C and is expressed as (Mallmann and O'Neill, 2013):

$$\begin{aligned}\log_{10} Kd_{Sc/Y}^{ol/melt} = {} & b_0 + b_1/T + b_2P/T + b_3Mg_{\#}^{ol}/T + b_4X_{CaO}^{melt}/T \\ & + b_5\left(X_{NaO_{0.5}}^{melt} + X_{KO_{0.5}}^{melt}\right)/T + b_6X_{SiO_2}^{melt}/T\end{aligned} \quad (2)$$

where $Kd_{Sc/Y}^{ol/melt}$ is Sc/Y exchange coefficient between olivine and melt; b_0 to b_6 are equation factors; T and P represent temperuature and pressure, respectively; Xs represent oxide molar content of melt.

Therefore, it is clear that the formula for the Al-in-olivine thermometer is related only to spinel Cr# and the Al partition coefficient between olivine and spinel (Coogan et al., 2014; Wan et al., 2008), whereas the formula of the Sc/Y partitioning thermometer is related to the olivine Fo value and the Sc/Y partition coefficient between olivine and its parental magma (Mallmann and O'Neill, 2013). Experimental diffusion studies have shown that Al and Cr in spinel (Suzuki et al., 2008) and Al in olivine (Spandler and O'Neill, 2010) are slow-diffusing elements, whereas Mg, Fe, Sc, and Y in olivine diffuse much more quickly (Spandler and O'Neill, 2010), as

confirmed by the relatively constant Al content from core to rim and the zoning profiles of Fo, Sc, and Y in the JGD olivine phenocrysts measured in this study (**Fig. 5 and 6**). To use the Sc/Y partitioning thermometer, we selected several discrete points from the olivine profile in **Fig. 6**. The temperatures calculated using the Al-in-olivine thermometer display a normal positive correlation with Fo content (**Fig. 10**), whereas the temperatures calculated with the Sc/Y partitioning olivine thermometer show a negative correlation with Fo content (**Fig. 10**). However, the temperatures calculated with both thermometers for the core composition are consistent with each other (around 1150 °C), which suggests that Fo, Sc, and Y in the core plateaus are less affected by diffusion. Thus, the Al-in-olivine thermometer is more resistant to diffusion than the Sc/Y partitioning thermometer.

Oxygen fugacity

Oxygen fugacity (fO_2) strongly affects the behavior of multivalent elements, which in turn affect many key processes, such as magma evolution, ore formation, and atmospheric compositional change (Cao et al., 2020; Frost, 1991; Mavrogenes and O'Neill, 1999; Putirka, 2016; Scholtysik and Canil, 2021; Snyder et al., 1993; Sun et al., 2015b; Wang et al., 2019; Wang et al., 2020). Therefore, many geochemical oxybarometers have been proposed to calculate oxygen fugacity (Ballhaus et al., 1991; Burnham and Berry, 2012; Mallmann and O'Neill, 2009; Mallmann and O'Neill, 2013; O'Neill and Wall, 1987; Rzehak et al., 2020; Smythe and Brenan, 2016). It is suggested that degassing plays an important role in controlling oxygen fugacity of

This is the peer-reviewed, final accepted version for American Mineralogist, published by the Mineralogical Society of America.
The published version is subject to change. Cite as Authors (Year) Title. American Mineralogist, in press.
DOI: https://doi.org/10.2138/am-2022-8567. http://www.minsocam.org/

basaltic magmas (Burgisser and Scaillet, 2007; Kelley and Cottrell, 2012; Mathez, 1984), though the study of de Moor et al. (2013) shows no change in $Fe^{3+}/\Sigma Fe$ or $S^{6+}/\Sigma S$ with extent of S degassing at Erta Ale volcano. Because olivine and spinel are the two early-crystallizing minerals in basaltic magma, oxybarometers based on olivine and spinel compositions record the fO_2 of the relatively primitive magma, as they are close to the liquidus. In this study, we used the widely applied olivine–spinel oxybarometer of Ballhaus et al. (1991) to constrain the oxygen fugacity of the JGD basaltic magma. The formula of the olivine–spinel oxybarometer of Ballhaus et al. (1991) is related to olivine Fo content and spinel composition and expressed as:

$$\Delta \log\left(fO_2\right)^{QFM} = 0.27 + \frac{2505}{T} - \frac{400P}{T} - 6\log\left(X_{Fe}^{Olv}\right) - \frac{3200\left(1 - X_{Fe}^{Olv}\right)^2}{T} + 2\log\left(X_{Fe^{2+}}^{Sp}\right) + 4\log\left(X_{Fe^{3+}}^{Sp}\right) + \frac{2630\left(X_{Al}^{Sp}\right)^2}{T} \quad (3)$$

where $\Delta \log\left(fO_2\right)^{QFM}$ is the calculated oxygen fugacity relative to QFM buffer; T and P represent temperature and pressure, respectively; X_{Fe}^{Olv} and $X_{Fe^{2+}}^{Sp}$ are molar ratios of $Fe^{2+}/(Fe^{2+} + Mg)$ in olivine and spinel; $X_{Fe^{3+}}^{Sp}$ and X_{Al}^{Sp} are molar ratios of $Fe^{3+}/(Fe+Al+Cr)^{3+}$ and $Al/(Fe+Al+Cr)^{3+}$, respectively. As the equation shows, the olivine–spinel oxybarometer needs Fe^{3+} content of spinel. Therefore, this oxybarometer may not be applicable to reduction systems because of too low Fe^{3+} for accurate determination in spinel.

Because the JGD spinel crystals measured in this study were too small (mostly 10–20 μm) to perform profile quantitative analysis to show whether they have Mg and Fe zoning (Vogt et al., 2015) and the BSE images of JGD olivine-hosted spinels

displayed little zonation (**Fig. S6**), we considered only the influence of Fo diffusion in olivine on the oxygen fugacity calculation. Discrete points on the Fo profiles from core to rim were selected to calculate oxygen fugacity. The results calculated with the Fo compositions of the core plateaus display oxidized oxygen fugacity, with fO_2 between QFM + 0.6 (QFM refers to the quartz–fayalite–magnetite buffer) and QFM + 2.0, and an average value of QFM + 1.4 (**Fig. 11**). As the used Fo contents are taken progressively from core to rim, the calculated fO_2 becomes accordingly reduced. Using the olivine rim compositions (assuming Fo = 70), the calculated values of fO_2 are between QFM − 0.9 and QFM + 0.8, with an average value of QFM + 0.1. Because the Fo contents of the olivine cores have relatively constant plateaus, we presume that the values of fO_2 calculated with the core compositions represent the true oxygen fugacity, whereas the lower fO_2 values calculated with the rim compositions were affected by Fo diffusion in the olivine phenocrysts.

H_2O content in JGD magma

Owing to degassing processes during magma upwelling and eruption, it is difficult to directly measure the primary H_2O content in volcanic rocks. Some hygrometers based on mineral geochemistry have been proposed by previous studies. For example, many studies have measured H_2O content in clinopyroxene and used the partitioning coefficient of H_2O between clinopyroxene and melt to calculate the H_2O content in magma (Liu et al., 2017; Nazzareni et al., 2011; Wade et al., 2008; Xia et al., 2013). Recently, Gavrilenko et al. (2016) calibrated a Ca-in-olivine

466 geohygrometer up to ~ 8 wt% H_2O content based on the partitioning of Ca between
467 olivine and silicate melt. We used this geohygrometer to calculate the H_2O content in
468 JGD magma. Although this geohygrometer does not consider the effect of other
469 volatiles (e.g., CO_2) and pressure on Ca partitioning coefficient and may not be
470 applicable to some magmatic systems (e.g., komatiite; De hoog et al., 2010;
471 Gavrilenko et al., 2016), it does not influence the discussion of the elemental diffusion
472 effect on this geohygrometer. The results show that as Ca content increases from core
473 to rim (**Fig. 12**), the calculated H_2O content decreases from ~4 wt.% to <2 wt.% (**Fig.**
474 **12**). Because Ca has a plateau in the core, the calculated H_2O content also displays a
475 plateau (~4 wt.%), which is treated as the primary H_2O content in the JGD magma.
476
477 **IMPLICATIONS**
478 Compared with MORB, the low olivine crystallization temperature (1150 °C),
479 high oxygen fugacity (QFM + 1.4), and high H_2O contents (~4 wt%) of the JGD
480 basalts support a metasomatized mantle source, which may have been related to the
481 closure of the Mongolia–Okhotsk Ocean or the subduction of the Paleo-Pacific Plate
482 beneath the Eurasian continent (Fan et al., 2003; Sun et al., 2015a; Tang et al., 2018;
483 Xu et al., 2013). The released fluids from subducted slabs metasomatized the
484 overlying mantle wedge and lowered the solidus of the wedge. Then, partial melting
485 of this metasomatized mantle wedge resulted in H_2O-enriched and high-oxygen-
486 fugacity magma, like that of the JGD basalts. As discussed above, the compositional
487 zoning of the olivine phenocrysts indicates a recharge magma system, which led to

488 the eruption of the JGD basalts or a deep magma carrying high-Fo olivines mixed
489 with a shallower and evolved magma. In the recharge model, the last input of evolved
490 magma induced an increase in the pressure of the JGD magma chamber. After a
491 timescale of dozens of days to less than two years, the JGD magma was erupted, and
492 the olivine phenocrysts preserved the disequilibrium compositional zoning.

493 Olivine phenocrysts from the JGD basalts show compositional zoning caused by
494 elemental diffusion. Modellings of the one-dimensional Mg–Fe and Ni diffusion
495 profiles indicate that the diffusion timescale is dozens of days to less than two years.
496 The diffusions of Mg, Ca, Fe, Sc, and Y in the JGD olivines have a strong influence
497 on magmatic temperature calculated using a Sc/Y-in-olivine thermometer, magmatic
498 oxygen fugacity calculated using an olivine–spinel oxybarometer, and magmatic H_2O
499 content calculated using a hygrometer based on Ca partitioning between olivine and
500 melt. However, the compositional plateaus in olivine cores, which were not
501 influenced by elemental diffusion, preserve the magmatic temperature (1150 °C),
502 oxygen fugacity (QFM + 1.4), and H_2O content (4 wt.%) that prevailed during the
503 formation of the JGD olivines, supporting the inference that the mantle source of the
504 JGD basalts was metasomatized by fluids released from a subducted slab. Our study
505 clearly shows that the use of olivine geochemistry to investigate magmatic
506 thermodynamic conditions must consider the effects of elemental diffusion. For
507 volcanic rocks, although they cool down soon after eruption, elemental profile
508 analyses of phenocrysts are needed to evaluate the effect of diffusion. If phenocrysts
509 have compositional plateaus in their cores, then the thermodynamic conditions of

510 primitive magma can be derived from the core compositions. For large intrusions, the
511 cooling rates normally vary from 200 ^{o}C/Ma to 1-10 ^{o}C/Ma (Ortega-Gutiérrez et al.,
512 2014), much smaller than that for volcanic rocks. Except for the very slow-diffusing
513 elements (e.g., P in olivine, CaAl-NaSi in plagioclase), other elements possibly reach
514 equilibrium at low temperature and thus loss the thermodynamic information of their
515 primitive magmas.
516

517 **ACKNOWLEDGEMENTS AND FUNDING**

518 The authors would like to thank Lin-Li Chen (GIG) for assistance with EPMA
519 analysis. This manuscript benefited much from the very constructive comments from
520 Diego González-García, Joe Boro, Marco Brenna and an anonymous reviewer. This
521 study was financially supported by the National Key Research and Development
522 Program of China (2018YFA0702600), Guangdong Basic and Applied Basic
523 Research Foundation (2021A1515017789) and the Program of Guangzhou City
524 (202102020614).
525

526 **REFERENCES CITED**

527 Abraham, A.-C., Francis, D., and Polvé, M. (2001) Recent alkaline basalts as probes
528 of the lithospheric mantle roots of the Northern Canadian Cordillera. Chemical
529 Geology, 175(3), 361-386.
530 Albert, H., Costa, F., Di Muro, A., Herrin, J., Métrich, N., and Deloule, E. (2019)
531 Magma interactions, crystal mush formation, timescales, and unrest during
532 caldera collapse and lateral eruption at ocean island basaltic volcanoes (Piton
533 de la Fournaise, La Réunion). Earth and Planetary Science Letters, 515, 187-

199.

Arai, S. (1994) Characterization of spinel peridotites by olivine-spinel compositional relationships: Review and interpretation. Chemical Geology, 113(3), 191-204.

Ballhaus, C., Berry, R.F., and Green, D.H. (1991) High pressure experimental calibration of the olivine-orthopyroxene-spinel oxygen geobarometer: implications for the oxidation state of the upper mantle. Contributions to Mineralogy and Petrology, 107(1), 27-40.

Batanova, V.G., Thompson, J.M., Danyushevsky, L.V., Portnyagin, M.V., Garbe-Schönberg, D., Hauri, E., Kimura, J.-I., Chang, Q., Senda, R., Goemann, K., Chauvel, C., Campillo, S., Ionov, D.A., and Sobolev, A.V. (2019) New Olivine Reference Material for In Situ Microanalysis. Geostandards and Geoanalytical Research, 43(3), 453-473.

Boro, J.R., Wolff, J.A., Neill, O.K., Steiner, A.R., and Ramos, F.C. (2021) Titanium diffusion profiles and melt inclusion chemistry and morphology in quartz from the Tshirege Member of the Bandelier Tuff. American Mineralogist, 106(4), 620-632.

Brenna, M., Cronin, S.J., Smith, I.E.M., Tollan, P.M.E., Scott, J.M., Prior, D.J., Bambery, K., and Ukstins, I.A. (2018) Olivine xenocryst diffusion reveals rapid monogenetic basaltic magma ascent following complex storage at Pupuke Maar, Auckland Volcanic Field, New Zealand. Earth and Planetary Science Letters, 499, 13-22.

Burgisser, A., and Scaillet, B. (2007) Redox evolution of a degassing magma rising to the surface. Nature, 445(7124), 194-197.

Burnham, A.D., and Berry, A.J. (2012) An experimental study of trace element partitioning between zircon and melt as a function of oxygen fugacity. Geochimica et Cosmochimica Acta, 95, 196-212.

Canil, D. (1997) Vanadium partitioning and the oxidation state of Archaean komatiite magmas. Nature, 389(6653), 842-845.

Cao, Y., Wang, C.Y., and Wei, B. (2019) Magma oxygen fugacity of Permian to

563 Triassic Ni-Cu sulfide-bearing mafic-ultramafic intrusions in the central Asian
564 orogenic belt, North China. Journal of Asian Earth Sciences, 173, 250-262.
565 -. (2020) Magma oxygen fugacity of mafic-ultramafic intrusions in convergent margin
566 settings: Insights for the role of magma oxidation states on magmatic Ni-Cu
567 sulfide mineralization. American Mineralogist, 105(12), 1841-1856.
568 Cherniak, D.J., and Watson, E.B. (1994) A study of strontium diffusion in plagioclase
569 using Rutherford backscattering spectroscopy. Geochimica et Cosmochimica
570 Acta, 58(23), 5179-5190.
571 Coogan, L.A., Saunders, A.D., and Wilson, R.N. (2014) Aluminum-in-olivine
572 thermometry of primitive basalts: Evidence of an anomalously hot mantle
573 source for large igneous provinces. Chemical Geology, 368, 1-10.
574 Costa, F., Dohmen, R., and Chakraborty, S. (2008) Time Scales of Magmatic
575 Processes from Modeling the Zoning Patterns of Crystals. Reviews in
576 Mineralogy and Geochemistry, 69(1), 545-594.
577 Costa, F., and Dungan, M. (2005) Short time scales of magmatic assimilation from
578 diffusion modeling of multiple elements in olivine. Geology, 33(10), 837-840.
579 Costa, F., Shea, T., and Ubide, T. (2020) Diffusion chronometry and the timescales of
580 magmatic processes. Nature Reviews Earth & Environment, 1(4), 201-214.
581 Danyushevsky, L.V., Perfit, M.R., Eggins, S.M., and Falloon, T.J. (2003) Crustal
582 origin for coupled 'ultra-depleted' and 'plagioclase' signatures in MORB
583 olivine-hosted melt inclusions: evidence from the Siqueiros Transform Fault,
584 East Pacific Rise. Contributions to Mineralogy and Petrology, 144(5), 619-637.
585 De Hoog, J.C.M., Gall, L., and Cornell, D.H. (2010) Trace-element geochemistry of
586 mantle olivine and application to mantle petrogenesis and
587 geothermobarometry. Chemical Geology, 270(1), 196-215.
588 de Moor, J.M., Fischer, T.P., Sharp, Z.D., King, P.L., Wilke, M., Botcharnikov, R.E.,
589 Cottrell, E., Zelenski, M., Marty, B., Klimm, K., Rivard, C., Ayalew, D.,
590 Ramirez, C., and Kelley, K.A. (2013) Sulfur degassing at Erta Ale (Ethiopia)
591 and Masaya (Nicaragua) volcanoes: Implications for degassing processes and

592 oxygen fugacities of basaltic systems. Geochem. Geophys. Geosyst., 14(10),
593 4076-4108.
594 Dohmen, R., Becker, H.-W., and Chakraborty, S. (2007) Fe–Mg diffusion in olivine I:
595 experimental determination between 700 and 1,200°C as a function of
596 composition, crystal orientation and oxygen fugacity. Physics and Chemistry
597 of Minerals, 34(6), 389-407.
598 Dohmen, R., and Chakraborty, S. (2007) Fe–Mg diffusion in olivine II: point defect
599 chemistry, change of diffusion mechanisms and a model for calculation of
600 diffusion coefficients in natural olivine. Physics and Chemistry of Minerals,
601 34(6), 409-430.
602 Elburg, M.A., Kamenetsky, V.S., Foden, J.D., and Sobolev, A. (2007) The origin of
603 medium-K ankaramitic arc magmas from Lombok (Sunda arc, Indonesia):
604 Mineral and melt inclusion evidence. Chemical Geology, 240(3), 260-279.
605 Fan, W.-M., Guo, F., Wang, Y.-J., and Lin, G. (2003) Late Mesozoic calc-alkaline
606 volcanism of post-orogenic extension in the northern Da Hinggan Mountains,
607 northeastern China. Journal of Volcanology and Geothermal Research, 121(1),
608 115-135.
609 Fisk, M., and Kelley, K.A. (2002) Probing the Pacific's oldest MORB glass: mantle
610 chemistry and melting conditions during the birth of the Pacific Plate. Earth
611 and Planetary Science Letters, 202(3), 741-752.
612 Frost, B.R. (1991) Introduction to oxygen fugacity and its petrologic importance.
613 Reviews in Mineralogy and Geochemistry, 25(1), 1-9.
614 Gavrilenko, M., Herzberg, C., Vidito, C., Carr, M.J., Tenner, T., and Ozerov, A. (2016)
615 A Calcium-in-Olivine Geohygrometer and its Application to Subduction Zone
616 Magmatism. Journal of Petrology, 57(9), 1811-1832.
617 Girona, T., and Costa, F. (2013) DIPRA: A user-friendly program to model multi-
618 element diffusion in olivine with applications to timescales of magmatic
619 processes. Geochemistry, Geophysics, Geosystems, 14(2), 422-431.
620 Gordeychik, B., Churikova, T., Shea, T., Kronz, A., Simakin, A., and Wörner, G.

(2020) Fo and Ni Relations in Olivine Differentiate between Crystallization and Diffusion Trends. Journal of Petrology, 61(9).

Herd, C.D.K. (2008) Basalts as Probes of Planetary Interior Redox State. Reviews in Mineralogy and Geochemistry, 68(1), 527-553.

Herzberg, C. (2011a) Basalts as temperature probes of Earth's mantle. Geology, 39(12), 1179-1180.

Herzberg, C. (2011b) Identification of Source Lithology in the Hawaiian and Canary Islands: Implications for Origins. Journal of Petrology, 52(1), 113-146.

Hofmann, A.W. (2003) Sampling mantle heterogeneity through oceanic basalts: isotopes and trace elements. In: Carlson, R. (Ed.), Geochemistry of the mantle and core, Treatise of Geochemistry, 2, 61-101.

Hong, L.-B., Xu, Y.-G., Ren, Z.-Y., Kuang, Y.-S., Zhang, Y.-L., Li, J., Wang, F.-Y. and Zhang, H.J.L. (2012) Petrology, geochemistry and Re–Os isotopes of peridotite xenoliths from Yantai, Shandong Province: Evidence for Phanerozoic lithospheric mantle beneath eastern North China Craton. Lithos, 155, 256-271.

Hong, L.-B., Zhang, Y.-H., Qian, S.-P., Liu, J.-Q., Ren, Z.-Y. and Xu, Y.-G. (2013) Constraints from melt inclusions and their host olivines on the petrogenesis of Oligocene-Early Miocene Xindian basalts, Chifeng area, North China Craton. Contributions to Mineralogy and Petrology, 165, 305-326.

Hong, L.-B., Zhang, Y.-H., Xu, Y.-G., Ren, Z.-Y., Yan, W., Ma, Q., Ma, L., and Xie, W. (2017) Hydrous orthopyroxene-rich pyroxenite source of the Xinkailing high magnesium andesites, Western Liaoning: Implications for the subduction-modified lithospheric mantle and the destruction mechanism of the North China Craton. Lithos, 282-283, 10-22.

Howarth, G.H., and Gross, J. (2019) Diffusion-controlled and concentric growth zoning revealed by phosphorous in olivine from rapidly ascending kimberlite magma, Benfontein, South Africa. Geochimica et Cosmochimica Acta, 266, 292-306.

650 Howarth, G.H., and Harris, C. (2017) Discriminating between pyroxenite and
651 peridotite sources for continental flood basalts (CFB) in southern Africa using
652 olivine chemistry. Earth and Planetary Science Letters, 475, 143-151.
653 Kahl, M., Chakraborty, S., Costa, F., and Pompilio, M. (2011) Dynamic plumbing
654 system beneath volcanoes revealed by kinetic modeling, and the connection to
655 monitoring data: An example from Mt. Etna. Earth and Planetary Science
656 Letters, 308(1), 11-22.
657 Kamenetsky, V.S., Elurg, M., Arculus, R., and Thomas, R. (2006) Magmatic origin
658 of low-Ca olivine in subduction-related magmas: co-existence of contrasting
659 magmas. Chemical Geology, 233, 346-357.
660 Kelley, K.A., and Cottrell, E. (2012) The influence of magmatic differentiation on the
661 oxidation state of Fe in a basaltic arc magma. Earth and Planetary Science
662 Letters, 329-330, 109-121.
663 Liu, J., Xia, Q.-K., Kuritani, T., Hanski, E., and Yu, H.-R. (2017) Mantle hydration
664 and the role of water in the generation of large igneous provinces. Nature
665 Communications, 8(1), 1824.
666 Liu, Y., Hu, Z., Gao, S., Günther, D., Xu, J., Gao, C., and Chen, H. (2008) In situ
667 analysis of major and trace elements of anhydrous minerals by LA-ICP-MS
668 without applying an internal standard. Chemical Geology, 257(1), 34-43.
669 Liu, Z., Shea, J.J., Foley, S.F., Bussweiler, Y., Rohrbach, A., Klemme, S. and Berndt, J.
670 (2021) Clarifying source assemblages and metasomatic agents for basaltic
671 rocks in eastern Australia using olivine phenocryst compositions. Lithos, 390,
672 106122.
673 Longpré, M.-A., Klügel, A., Diehl, A., and Stix, J. (2014) Mixing in mantle magma
674 reservoirs prior to and during the 2011–2012 eruption at El Hierro, Canary
675 Islands. Geology, 42(4), 315-318.
676 Luo, Q.-C., Ren, Z.-Y., Zhang, L., and Xu, X.-B. (2020) Petrogenesis and deep
677 dynamic geological processes of Mesozoic basalts from the northern Great
678 Xing'an Ridge Geochimica, 49(2), 168-192 (in Chinese with English abstract).

679 Lynn, K.J., Garcia, M.O., Shea, T., Costa, F., and Swanson, D.A. (2017) Timescales of
680 mixing and storage for Keanakāko‘i Tephra magmas (1500–1820 C.E.),
681 Kīlauea Volcano, Hawai‘i. Contributions to Mineralogy and Petrology, 172(9),
682 76.
683 Lynn, K.J., Shea, T., Garcia, M.O., Costa, F., and Norman, M.D. (2018) Lithium
684 diffusion in olivine records magmatic priming of explosive basaltic eruptions.
685 Earth and Planetary Science Letters, 500, 127-135.
686 Mallmann, G., and O’Neill, H.S.C. (2009) The Crystal/Melt Partitioning of V during
687 Mantle Melting as a Function of Oxygen Fugacity Compared with some other
688 Elements (Al, P, Ca, Sc, Ti, Cr, Fe, Ga, Y, Zr and Nb). Journal of Petrology,
689 50(9), 1765-1794.
690 Mallmann, G., and O’Neill, H.S.C. (2013) Calibration of an Empirical Thermometer
691 and Oxybarometer based on the Partitioning of Sc, Y and V between Olivine
692 and Silicate Melt. Journal of Petrology, 54(5), 933-949.
693 Mathez, E.A. (1984) Influence of degassing on oxidation states of basaltic magmas.
694 Nature, 310(5976), 371-375.
695 Matthews, S., Shorttle, O., and Maclennan, J. (2016) The temperature of the Icelandic
696 mantle from olivine-spinel aluminum exchange thermometry. Geochemistry,
697 Geophysics, Geosystems, 17(11), 4725-4752.
698 Mavrogenes, J.A., and O’Neill, H.S.C. (1999) The relative effects of pressure,
699 temperature and oxygen fugacity on the solubility of sulfide in mafic magmas.
700 Geochimica et Cosmochimica Acta, 63(7), 1173-1180.
701 Muller, W., Shelley, M., Miller, P., and Broude, S. (2009) Initial performance metrics
702 of a new custom-designed ArF excimer LA-ICPMS system coupled to a two-
703 volume laser-ablation cell. Journal of Analytical Atomic Spectrometry, 24(2),
704 209-214.
705 Mutch, E.J.F., Maclennan, J., Shorttle, O., Edmonds, M., and Rudge, J.F. (2019)
706 Rapid transcrustal magma movement under Iceland. Nature Geoscience, 12(7),
707 569-574.

708 Nazarova, D.P., Portnyagin, M.V., Krasheninnikov, S.P., Mironov, N.L., and Sobolev,
709 A.V. (2017) Initial H2O content and conditions of parent magma origin for
710 Gorely volcano (Southern Kamchatka) estimated by trace element
711 thermobarometry. Doklady Earth Sciences, 472(1), 100-103.
712 Nazzareni, S., Skogby, H., and Zanazzi, P.F. (2011) Hydrogen content in
713 clinopyroxene phenocrysts from Salina mafic lavas (Aeolian arc, Italy).
714 Contributions to Mineralogy and Petrology, 162(2), 275-288.
715 O'Neill, H.S.C., and Wall, V.J. (1987) The Olivine—Orthopyroxene—Spinel Oxygen
716 Geobarometer, the Nickel Precipitation Curve, and the Oxygen Fugacity of the
717 Earth's Upper Mantle. Journal of Petrology, 28(6), 1169-1191.
718 Oeser, M., Dohmen, R., Horn, I., Schuth, S., and Weyer, S. (2015) Processes and time
719 scales of magmatic evolution as revealed by Fe–Mg chemical and isotopic
720 zoning in natural olivines. Geochimica et Cosmochimica Acta, 154, 130-150.
721 Ortega-Gutiérrez, F., Elías-Herrera, M., Morán-Zenteno, D.J., Solari, L., Luna-
722 González, L., and Schaaf, P. (2014) A review of batholiths and other plutonic
723 intrusions of Mexico. Gondwana Research, 26(3), 834-868.
724 Petry, C., Chakraborty, S., and Palme, H. (2004) Experimental determination of Ni
725 diffusion coefficients in olivine and their dependence on temperature,
726 composition, oxygen fugacity, and crystallographic orientation. Geochimica et
727 Cosmochimica Acta, 68(20), 4179-4188.
728 Putirka, K. (2016) Rates and styles of planetary cooling on Earth, Moon, Mars, and
729 Vesta, using new models for oxygen fugacity, ferric-ferrous ratios, olivine-
730 liquid Fe-Mg exchange, and mantle potential temperature. American
731 Mineralogist, 101(4), 819-840.
732 Qian, Q., O'Neill, H.S.C., and Hermann, J. (2010) Comparative diffusion coefficients
733 of major and trace elements in olivine at ~950 °C from a xenocryst included in
734 dioritic magma. Geology, 38(4), 331-334.
735 Ruprecht, P., and Plank, T. (2013) Feeding andesitic eruptions with a high-speed
736 connection from the mantle. Nature, 500(7460), 68-72.

737 Rzehak, L.J.A., Rohrbach, A., Vollmer, C., Höfer, H.E., Berndt, J., and Klemme, S.
738 (2020) Ferric-ferrous iron ratios of experimental majoritic garnet and
739 clinopyroxene as a function of oxygen fugacity. American Mineralogist,
740 105(12), 1866-1874.
741 Søager, N., Portnyagin, M., Hoernle, K., Holm, P.M., Hauff, F., and Garbe-Schönberg,
742 D. (2015) Olivine Major and Trace Element Compositions in Southern
743 Payenia Basalts, Argentina: Evidence for Pyroxenite–Peridotite Melt Mixing
744 in a Back-arc Setting. Journal of Petrology, 56(8), 1495-1518.
745 Schiano, P. (2003) Primitive mantle magmas recorded as silicate melt inclusions in
746 igneous minerals. Earth-Science Reviews, 63(1-2), 121-144.
747 Scholtysik, R., and Canil, D. (2021) The effects of S, Cl and oxygen fugacity on the
748 sublimation of volatile trace metals degassed from silicate melts with
749 implications for volcanic emissions. Geochimica et Cosmochimica Acta, 301,
750 141-157.
751 Shea, T., Costa, F., Krimer, D., and Hammer, J.E. (2015a) Accuracy of timescales
752 retrieved from diffusion modeling in olivine: A 3D perspective. American
753 Mineralogist, 100, (10), 2026-2042.
754 Shea, T., Lynn, K.J., and Garcia, M.O. (2015b) Cracking the olivine zoning code:
755 Distinguishing between crystal growth and diffusion. Geology, 43(10), 935-
756 938.
757 Shearer, C.K., McKay, G., Papike, J.J., and Karner, J.M. (2006) Valence state
758 partitioning of vanadium between olivine-liquid: Estimates of the oxygen
759 fugacity of Y980459 and application to other olivine-phyric martian basalts.
760 American Mineralogist, 91(10), 1657-1663.
761 Shishkina, T.A., Portnyagin, M.V., Botcharnikov, R.E., Almeev, R.R., Simonyan, A.V.,
762 Garbe-Schönberg, D., Schuth, S., Oeser, M., and Holtz, F. (2018)
763 Experimental calibration and implications of olivine-melt vanadium
764 oxybarometry for hydrous basaltic arc magmas. American Mineralogist,
765 103(3), 369-383.

766 Simkin, T., and Smith, J.V. (1970) Minor-element distribution in olivine. Journal of
767 Geology, 78, 304-325.
768 Smythe, D.J., and Brenan, J.M. (2016) Magmatic oxygen fugacity estimated using
769 zircon-melt partitioning of cerium. Earth and Planetary Science Letters, 453,
770 260-266.
771 Snyder, D., Carmichael, I.S.E., and Wiebe, R.A. (1993) Experimental study of liquid
772 evolution in an Fe-rich, layered mafic intrusion: constraints of Fe-Ti oxide
773 precipitation on the T-fO2 and T-ϱ paths of tholeiitic magmas. Contributions to
774 Mineralogy and Petrology, 113(1), 73-86.
775 Sobolev, A.V., Hofmann, A.W., Sobolev, S.V., and Nikogosian, I.K. (2005) An
776 olivine-free mantle source of Hawaiian shield basalts. Nature, 434.
777 Spandler, C., and O'Neill, H.S.C. (2010) Diffusion and partition coefficients of minor
778 and trace elements in San Carlos olivine at 1,300°C with some geochemical
779 implications. Contributions to Mineralogy and Petrology, 159(6), 791-818.
780 Sun, M.-D., Xu, Y.-G., Wilde, S.A., and Chen, H.-L. (2015a) Provenance of
781 Cretaceous trench slope sediments from the Mesozoic Wandashan Orogen, NE
782 China: Implications for determining ancient drainage systems and tectonics of
783 the Paleo-Pacific. Tectonics, 34(6), 1269-1289.
784 Sun, W., Huang, R.-f., Li, H., Hu, Y.-b., Zhang, C.-c., Sun, S.-j., Zhang, L.-p., Ding,
785 X., Li, C.-y., Zartman, R.E., and Ling, M.-x. (2015b) Porphyry deposits and
786 oxidized magmas. Ore Geology Reviews, 65, 97-131.
787 Suzuki, A.M., Yasuda, A., and Ozawa, K. (2008) Cr and Al diffusion in chromite
788 spinel: experimental determination and its implication for diffusion creep.
789 Physics and Chemistry of Minerals, 35(8), 433.
790 Tang, J., Xu, W., Wang, F., and Ge, W. (2018) Subduction history of the Paleo-Pacific
791 slab beneath Eurasian continent: Mesozoic-Paleogene magmatic records in
792 Northeast Asia. Science China Earth Sciences, 61(5), 527-559.
793 Thomson, A., and Maclennan, J. (2013) The Distribution of Olivine Compositions in
794 Icelandic Basalts and Picrites. Journal of Petrology, 54(4), 745-768.

Vogt, K., Dohmen, R., and Chakraborty, S. (2015) Fe-Mg diffusion in spinel: New experimental data and a point defect model†. American Mineralogist, 100(10), 2112-2122.

Wade, J.A., Plank, T., Hauri, E.H., Kelley, K.A., Roggensack, K., and Zimmer, M. (2008) Prediction of magmatic water contents via measurement of H2O in clinopyroxene phenocrysts. Geology, 36(10), 799-802.

Wan, Z., Coogan, L.A., and Canil, D. (2008) Experimental calibration of aluminum partitioning between olivine and spinel as a geothermometer. American Mineralogist, 93(7), 1142-1147.

Wang, F., Zhou, X.-H., Zhang, L.-C., Ying, J.-F., Zhang, Y.-T., Wu, F.-Y., and Zhu, R.-X. (2006) Late Mesozoic volcanism in the Great Xing'an Range (NE China): Timing and implications for the dynamic setting of NE Asia. Earth and Planetary Science Letters, 251(1), 179-198.

Wang, J., Xiong, X., Takahashi, E., Zhang, L., Li, L., and Liu, X. (2019) Oxidation State of Arc Mantle Revealed by Partitioning of V, Sc, and Ti Between Mantle Minerals and Basaltic Melts. Journal of Geophysical Research: Solid Earth, 124(5), 4617-4638.

Wang, J., Xiong, X., Zhang, L., and Takahashi, E. (2020) Element loss to platinum capsules in high-temperature–pressure experiments. American Mineralogist, 105(10), 1593-1597.

Wang, Y., Xu, F., Gauvin, R., Kong, M., Khan, M., Liu, Z., and Zeng, Y. (2017) Growth modes for monoclinic yttria-stabilized zirconia during the martensitic transformation. Journal of the American Ceramic Society, 100(10), 4874-4883.

Wilde, S.A. (2015) Final amalgamation of the Central Asian Orogenic Belt in NE China: Paleo-Asian Ocean closure versus Paleo-Pacific plate subduction — A review of the evidence. Tectonophysics, 662, 345-362.

Wilde, S.A., and Zhou, J.-B. (2015) The late Paleozoic to Mesozoic evolution of the eastern margin of the Central Asian Orogenic Belt in China. Journal of Asian Earth Sciences, 113, 909-921.

824 Wu, F.-Y., Sun, D.-Y., Ge, W.-C., Zhang, Y.-B., Grant, M.L., Wilde, S.A., and Jahn,
825 B.-M. (2011) Geochronology of the Phanerozoic granitoids in northeastern
826 China. Journal of Asian Earth Sciences, 41(1), 1-30.
827 Wu, S., Wu, Y., Yang, Y., Wang, H., Huang, C., Xie, L., and Yang, J. (2020)
828 Simultaneous Quantification of Forsterite Content and Minor–Trace Elements
829 in Olivine by LA–ICP–MS and Geological Applications in Emeishan Large
830 Igneous Province. Minerals, 10(7), 634.
831 Xia, Q.-K., Liu, J., Liu, S.-C., Kovács, I., Feng, M., and Dang, L. (2013) High water
832 content in Mesozoic primitive basalts of the North China Craton and
833 implications on the destruction of cratonic mantle lithosphere. Earth and
834 Planetary Science Letters, 361, 85-97.
835 Xiao, W., Kröner, A., and Windley, B. (2009) Geodynamic evolution of Central Asia
836 in the Paleozoic and Mesozoic. International Journal of Earth Sciences, 98(6),
837 1185-1188.
838 Xiao, W., Windley, B.F., Hao, J., and Zhai, M. (2003) Accretion leading to collision
839 and the Permian Solonker suture, Inner Mongolia, China: Termination of the
840 central Asian orogenic belt. Tectonics, 22(6).
841 Xu, W.-L., Pei, F.-P., Wang, F., Meng, E., Ji, W.-Q., Yang, D.-B., and Wang, W. (2013)
842 Spatial–temporal relationships of Mesozoic volcanic rocks in NE China:
843 Constraints on tectonic overprinting and transformations between multiple
844 tectonic regimes. Journal of Asian Earth Sciences, 74, 167-193.
845 Yang, F., Huang, X.-L., Xu, Y.-G., and He, P.-L. (2019) Plume-ridge interaction in the
846 South China Sea: Thermometric evidence from Hole U1431E of IODP
847 Expedition 349. Lithos, 324-325, 466-478.
848 Zhang, J.H., Ge, W.C., Wu, F.Y., Wilde, S.A., Yang, J.-H., and Liu, X.-M. (2008a)
849 Large-scale Early Cretaceous volcanic events in the northern Great Xing'an
850 Range, Northeastern China. Lithos, 102(1), 138-157.
851 Zhang, L., Qian, S.-P., Li, N., Hong, L.-B., Zhang, Y.-Q., and Ren, Z.-Y. (2021)
852 Simultaneous In Situ Determination of Pb Isotope Ratios and Trace Element

Concentrations in Melt Inclusions by LASS-ICP-MS. Geochemistry, Geophysics, Geosystems, 22(1), e2020GC009451.

Zhang, L., Ren, Z.-Y., Xia, X.-P., Yang, Q., Hong, L.-B., and Wu, D. (2019) In situ determination of trace elements in melt inclusions using laser ablation inductively coupled plasma sector field mass spectrometry. Rapid Communications in Mass Spectrometry, 33(4), 361-370.

Zhang, L.C., Zhou, X.-H., Ying, J.-F., Wang, F., Guo, F., Wan, B., and Chen, Z.-G. (2008b) Geochemistry and Sr–Nd–Pb–Hf isotopes of Early Cretaceous basalts from the Great Xinggan Range, NE China: Implications for their origin and mantle source characteristics. Chemical Geology, 256(1), 12-23.

Figure captions

Figure 1 (a) Simplified geological map of East Asia. (b) Distribution of the Cretaceous volcanic rocks in NE China. CAOB - Central Asian Orogenic Belt.

Figure 2 (a-b) Photomicrographs of representative samples under crossed-polarizers. The large olivine phenocryst in b was selected for LA-ICP-MS elemental mapping. (c) Image taken under reflected light of the same olivine phenocryst in b. (d) BSE image of the measured olivine phenocryst after LA-ICP-MS analysis. The crossed-polarizer image and BSE image show the zonation. Laser ablation was conducted under raster mode. Laser spot size, 45 μm; repetition rate, 15 Hz; energy density, 8 mJ cm^{-2}; moving speed 10 μm s^{-1}. Ol, olivine; MI, melt inclusion; Sp, spinel.

878

879 **Figure 3** Olivine forsterite (Fo) profiles measured by EPMA. All measured olivine
880 phenocrysts display normal Fo zoning pattern (decrease from core to rim).

881

882 **Figure 4** Histogram of Fo contents for olivine rims and cores. The dashed lines
883 indicate the mean values of Fo contents for rims and cores.

884

885 **Figure 5** 2D elemental distribution plots for selected elements in the olivine
886 phenocryst in Figure 2b. Except Fo in percentage, other elements are in ppm.

887

888 **Figure 6** Concentration variations for Fo and P_2O_5 (a), Al_2O_3 and Sc/Y (b) across the
889 profile indicated by the red line in the BSE image. The peak or trench represents crack
890 in the measured olivine phenocryst. Dashed lines in (a) are modeled Fo content
891 profiles with DIPRA program. The blue dashed line indicates the inferred initial
892 profile shape before diffusion occurred. The red dashed line shows a diffusion
893 timescale of about 400 days. Modelling parameters: temperature = 1092 ^{o}C; fO_2 =
894 ΔQFM + 1.4; crystal orientation (α, β, γ) = (84, 85, 7).

895

896 **Figure 7** Plot of Cr# in spinels vs Fo in their host olivines. The olivine-spinel mantle
897 array is from Arai (1994).

898

899 **Figure 8** Plots of concentrations (in ppm) of Ca (a) and Ni (b) vs Fo for the JGD

900 olivine cores.

901

902 **Figure 9** DIPRA modelling examples of rim-to-core Fo (a, b) and Ni (c, d) profiles
903 for the JGD olivines. BSE images illustrate the locations of the analytical traverses.
904 Red lines show the modelling results from one dimensional diffusion model for a
905 semi-infinite medium with calculated timescales. C_0 is the initial concentration and C_i
906 is the boundary concentration. The error bars of all measured NiO are set to 6%.

907

908 **Figure 10** Olivine crystallization temperatures calculated with the Al-in-olivine
909 thermometer by Coogan et al. (2014) (triangle) and by Sc/Y-in-olivine thermometer
910 by Mallmann and O'Neill (2013) (circle). The temperatures calculated by Al-in-
911 olivine thermometer show a normal positive correlation with Fo contents. In contrast,
912 the temperatures calculated by Sc/Y-in-olivine thermometer show a negative
913 correlation with Fo contents. The Sc/Y-in-olivine thermometer used the bulk rock
914 Sc/Y (Luo et al., 2020) to calculate the Sc/Y partition coefficient. Data source: MORB,
915 Matthews et al. (2016), Yang et al. (2019) and Danyushevsky et al. (2003); Arc,
916 Elburg et al. (2007), Søager et al. (2015) and Nazarova et al. (2017).

917

918 **Figure 11** Calculated oxygen fugacity relative to the QFM buffer vs Cr# in spinel.
919 The oxygen fugacity calculated with olivine core composition (circles) records the
920 true magmatic redox condition. Other symbols represent the results calculated with
921 the olivine compositions (Fo = 80, 75 and 70) influenced by Mg-Fe diffusion.

922

923 **Figure 12** Concentration variation of CaO for the A-A' profile in Figure 5a and the
924 calculated H_2O content with the Ca-in-olivine geohygrometer (Gavrilenko et al.,
925 2016). The MgO (7.06 wt%) and CaO (9.50 wt%) of the JGD whole rock (Luo et al.,
926 2020) were used in the calculation. The peak or trench represents a crack in the
927 measured olivine phenocryst.

928

This is the peer-reviewed, final accepted version for American Mineralogist, published by the Mineralogical Society of America.
The published version is subject to change. Cite as Authors (Year) Title. American Mineralogist, in press.
DOI: https://doi.org/10.2138/am-2022-8567. http://www.minsocam.org/

Figure 1

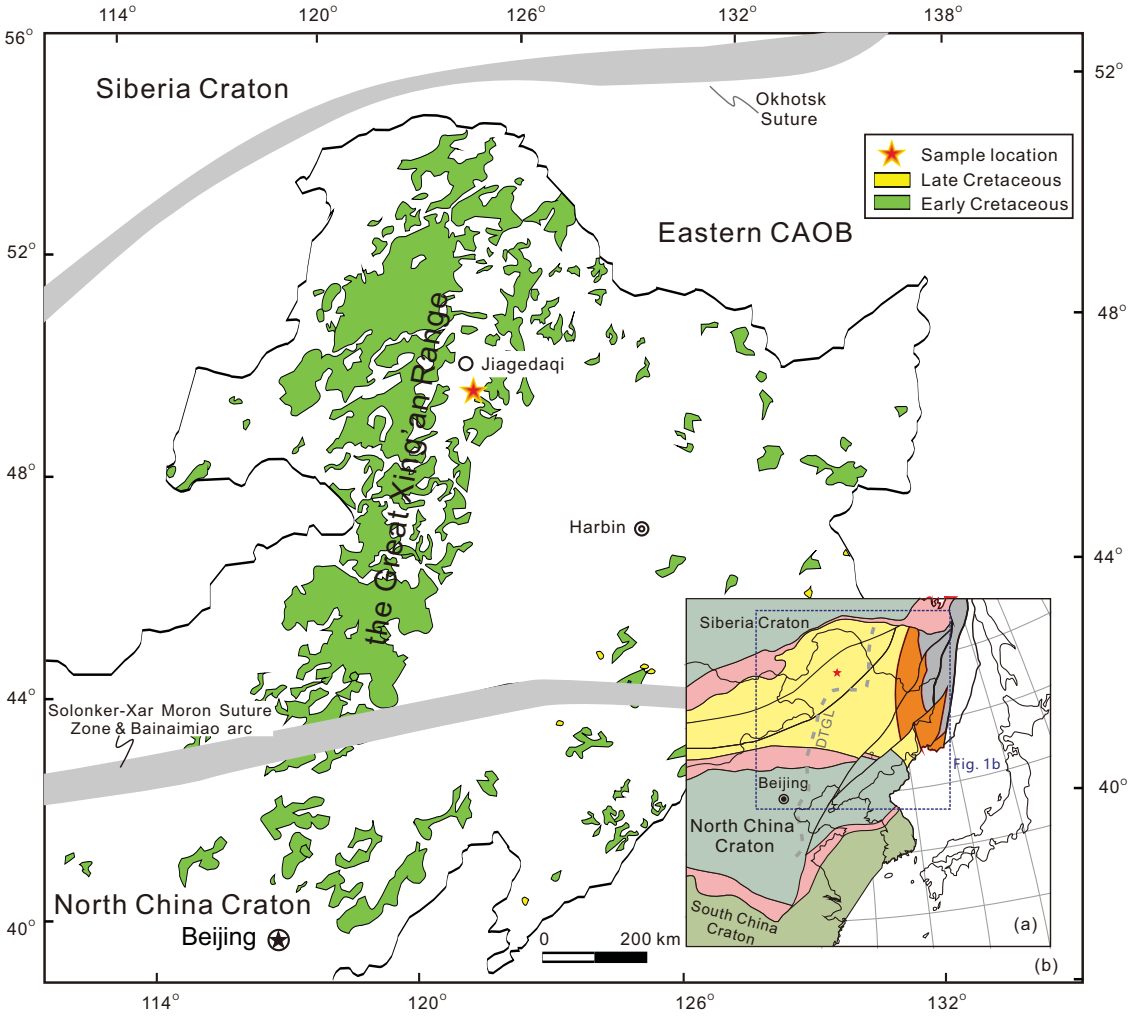

This is the peer-reviewed, final accepted version for American Mineralogist, published by the Mineralogical Society of America.
The published version is subject to change. Cite as Authors (Year) Title. American Mineralogist, in press.
DOI: https://doi.org/10.2138/am-2022-8567. http://www.minsocam.org/

Figure 2

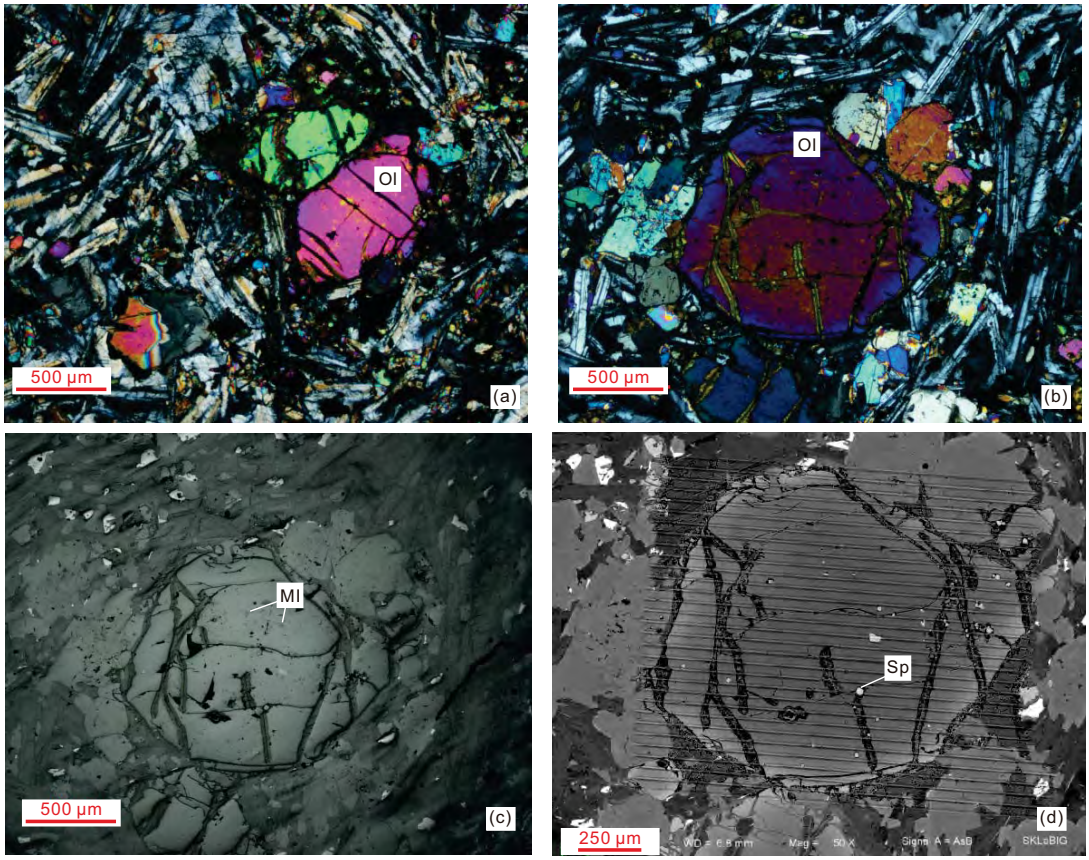

Figure 3

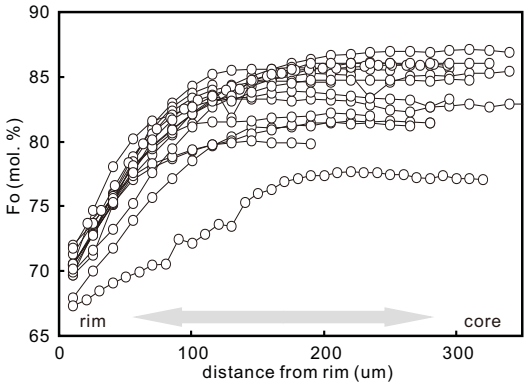

Figure 4

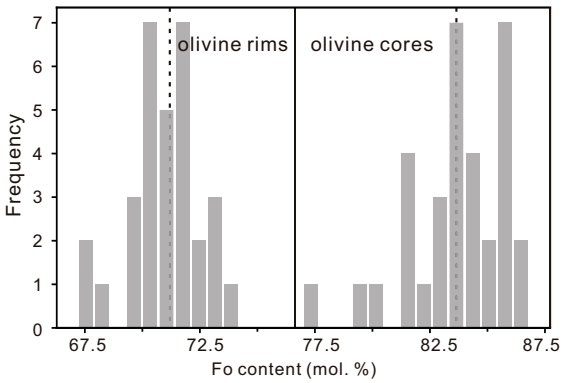

This is the peer-reviewed, final accepted version for American Mineralogist, published by the Mineralogical Society of America.
The published version is subject to change. Cite as Authors (Year) Title. American Mineralogist, in press.
DOI: https://doi.org/10.2138/am-2022-8567. http://www.minsocam.org/

Figure 5

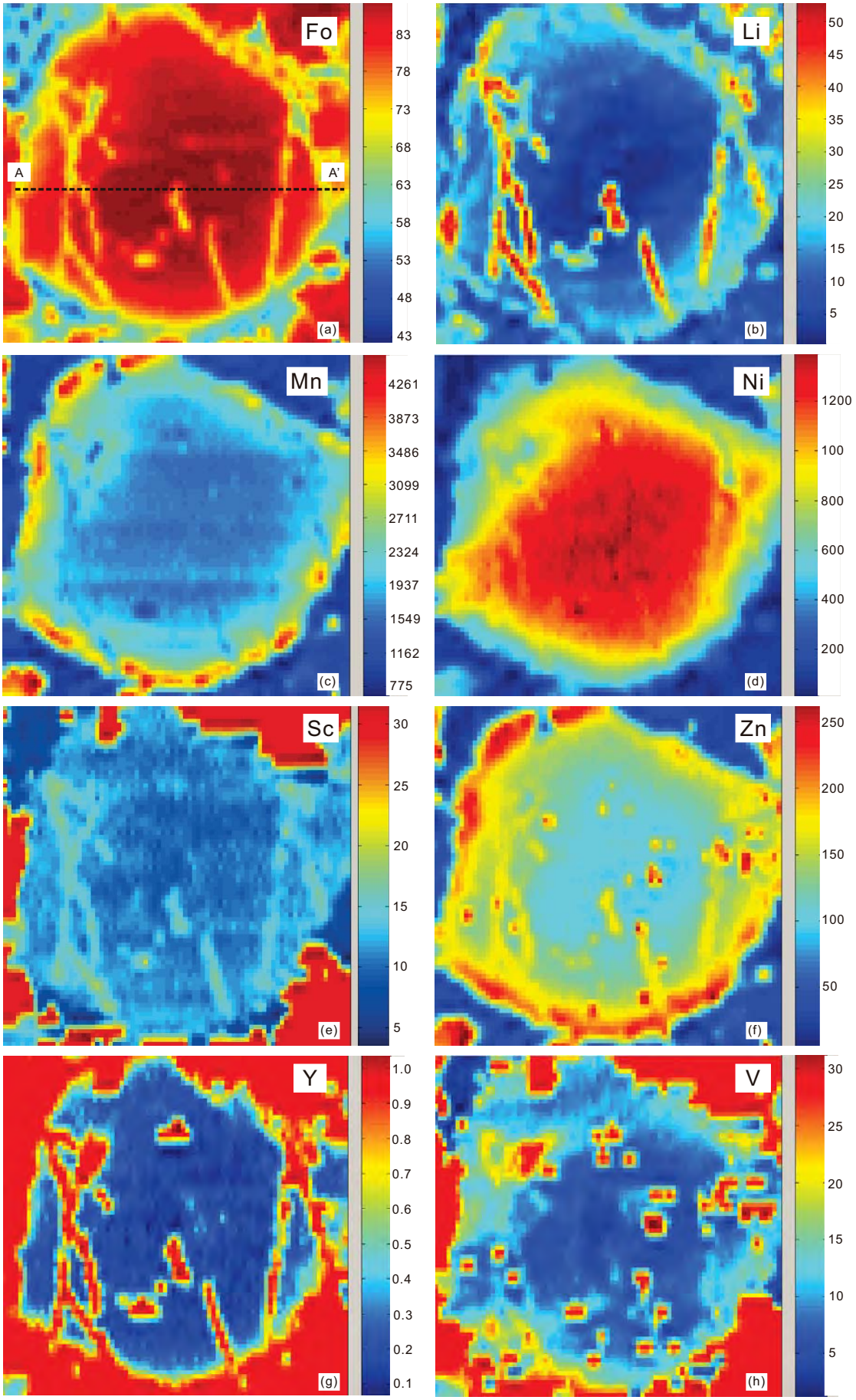

Figure 6

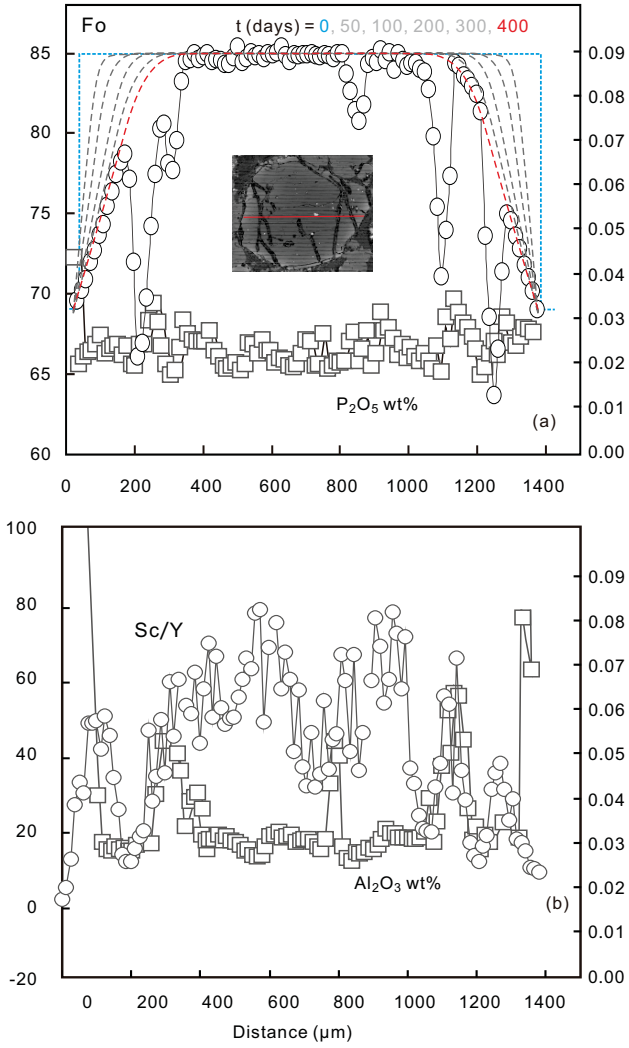

Figure 7

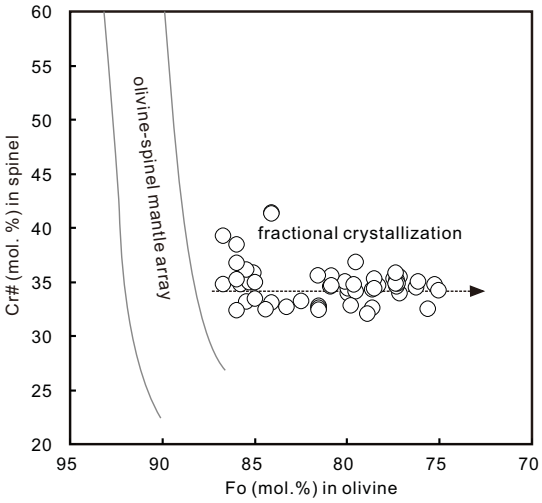

Figure 8

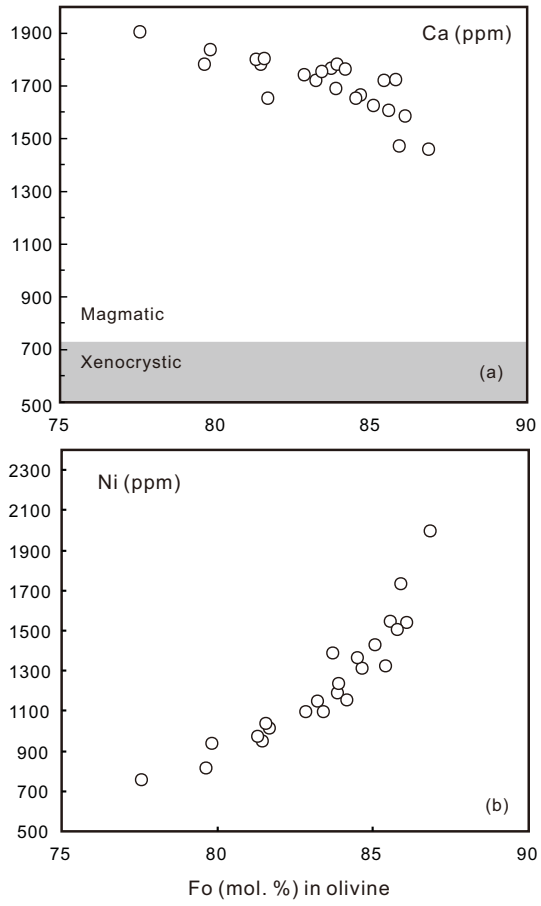

Figure 9

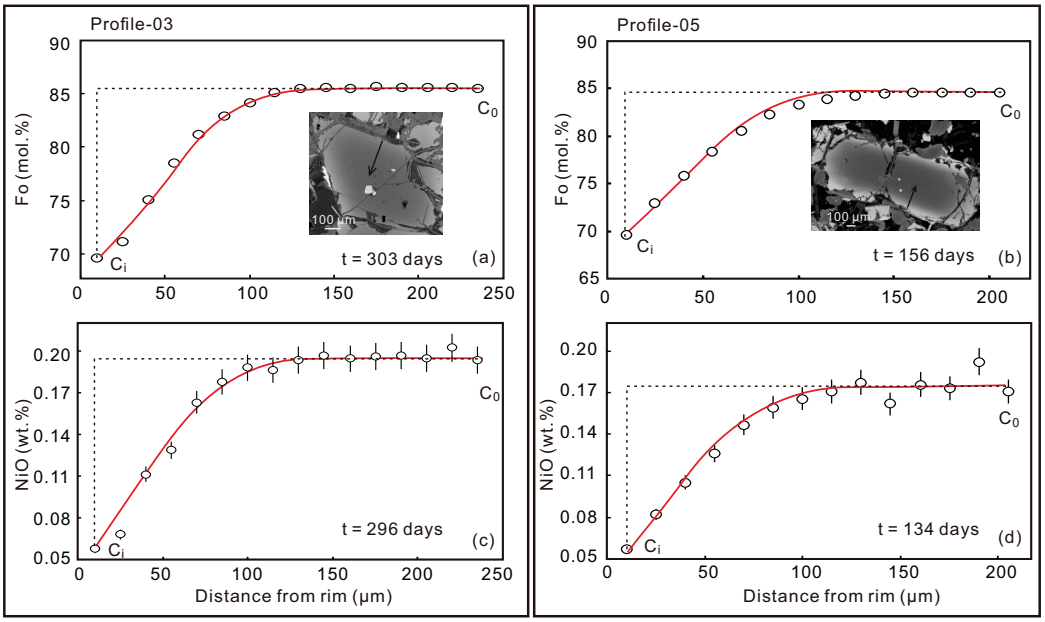

Figure 10

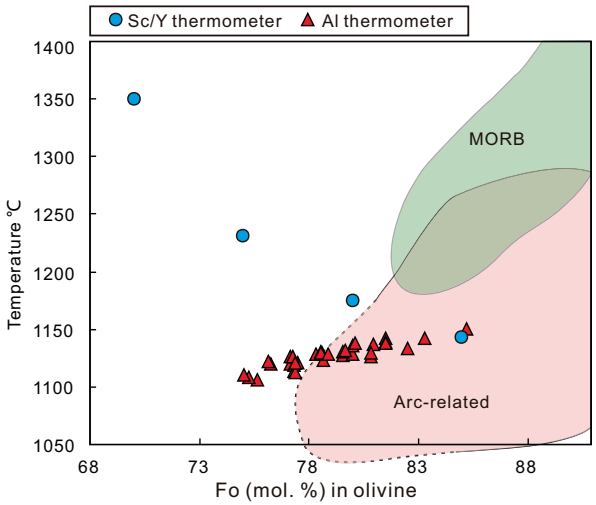

Figure 11

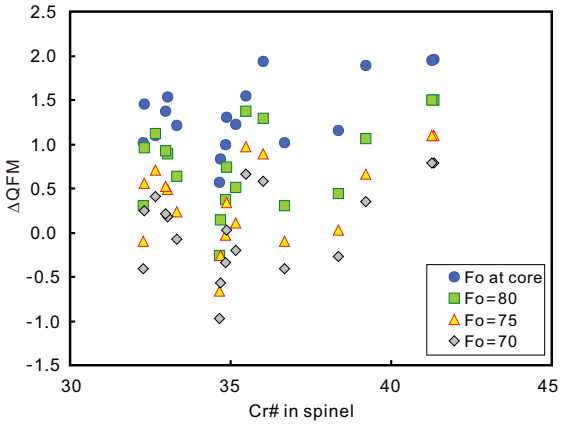

Figure 12